Numerical simulation of the initial particle parking structure of cement/geopolymer paste and the dissolution of amorphous silica using real-shape particles

Zuo, Yibing; Qian, Zhiwei; Garboczi, Edward J.; Ye, Guang

DOI
10.1016/j.conbuildmat.2018.07.063

Publication date
2018

Document Version
Accepted author manuscript

Published in
Construction and Building Materials

Construction and Building Materials 185(2018) 206-219

Numerical simulation of the initial particle parking structure of cement/geopolymer paste and the dissolution of amorphous silica using real-shape particles

Yibing Zuo[a], Zhiwei Qian[b], Edward J. Garboczi[c], Guang Ye[a]

[a] Section of Materials and Environment, Faculty of Civil Engineering and Geosciences, Delft University of Technology, Delft 2628CN, The Netherlands

[b] Section of Railway Engineering, Faculty of Civil Engineering and Geosciences, Delft University of Technology, Delft 2628CN, The Netherlands

[c] National Institute of Standards and Technology, Boulder, CO 80305, USA

Abstract: Many particle-based numerical models have been used to simulate the hydration process of cementitious materials. Most of those models employ regular shape particles, like the commonly used spheres, to represent cement, slag, or fly ash, which neglects the influence of particle shape. To deal with this issue, this study extended the Anm material model and used irregular shape particles to simulate the initial particle parking structures of cement/geopolymer pastes. The irregular shapes of cement, slag and fly ash particles were characterized by spherical harmonic series. Compared to the initial particle structures simulated using spherical particles, those using irregular shape particles had total surface areas and bulk specific surface areas with up to 37.40 % and 36.84 % larger, respectively. However, the pore size distributions of the simulated initial particle structures did not show significant influence of particle shape. As a demonstration to illustrate the influence of particle shape on dissolution, the initial particle parking structure of amorphous silica in alkaline solution was generated using irregular shape particles, and was used as input to simulate the dissolution of silica particles. The Lattice Boltzmann method was used to simulate the transport process of aqueous ions and thermodynamics was employed to consider the rate of dissolution of silica. The dissolved fractions of silica at different temperatures in the simulations agreed well with experimental measurements. The influences of continuous stirring, concentration of alkali and particle shape on the dissolution kinetics of silica were investigated numerically.

Keywords: numerical simulation; parking structure; cement/geopolymer paste; dissolution; amorphous silica; particle shape

Correspondent author: Yibing ZUO. **E-mail:** Y.Zuo@tudelft.nl. **Tel:** +31-152788343

1 Introduction

Many particle-based numerical models have been used to simulate the hydration process of cementitious materials [1-4]. In these models, regular shape particles, usually spherical particles, are used to represent the particles of cement, slag, or fly ash. However, the real particle shapes found in cement, slag and fly ash are irregular and non-spherical due to the manufacturing processes and particle grinding methods used. Spherical shapes have the minimum specific surface area (m^2/m^3) of any closed 3D shape [5], so the greater the particle deviates from sphericity, the greater the specific surface area it has. The greater specific surface area enables the particle to hydrate faster, since hydration is a surface-controlled set of reactions [6]. It is reported that variation in particle shape influences the reaction kinetics of cement hydration [4, 7].

An appropriate way to analytically characterize the shape of irregular shape particles is to make use of spherical harmonic series [8]. The spherical harmonic expansion coefficients can be obtained based on the digital images of particles from micro X-ray Computed Tomography scans [8]. Bullard and Garboczi used this technique to reconstruct real particle shapes of cement, and produced three-dimensional digitized cement paste microstructures using real-shape cement particles [7]. In their numerical model, the particles described by the spherical harmonic expansion coefficients were digitized into voxels, and then the digitized particles were parked into a predefined voxel cube. In such a way, however, the resolution of the simulated cement paste microstructure is constrained by the resolution used to digitize the particles, and the smallest particle that can be parked also depends on the digitization resolution. By implementing the spherical harmonic series, Qian et al. developed a geometrical model (denoted as the Anm material model) to park real-shape aggregates according to mortar or concrete particle size distributions [9]. The term “parking” is defined as placing a particle with random location and orientation without touching another particle [10]. After successful parking, the particle is fixed in place and the next particle is randomly parked. In the Anm model, the real-shape particles are directly parked into a predefined cube without prior digitization. Therefore, there are no limitations on the resolution of simulated initial particle structure and the smallest particle size. However, a wider particle size range implies that many more particles need to be parked to accurately represent the particle size distribution, which usually results in longer computation time. To increase the simulation efficiency, Stephen et al. improved the Anm model by integrating two new algorithms [11]. One is the extent overlap box (EOB) method that detects interparticle contact, and the other is the capability of adding a uniform-thickness shell to each particle. These two new algorithms, along with an integrated parallel processing programming interface, accelerate the particle placement/parking process.

In the original Anm material model, only one component, for example, one type of aggregates, is parked at one time [9, 11]. Therefore, it cannot simultaneously park particles from binary or multiple components, for example, two types of aggregates with different particle shape databases and mechanical properties. In most cementitious/geopolymer materials, blended materials are used, such as binary-blended cement with slag, or fly ash, and binary-blended slag with fly-ash-based geopolymer paste. In this study, the original Anm material model was extended to simulate the initial particle parking structures of binary-blended systems with components chosen from cement, slag, or fly ash. In the meantime, the initial particle parking structure of cement/geopolymer paste was also simulated with HYMOSTRUC3D [4, 12, 13] using spherical particles for comparisons. The initial particle parking structures, simulated using real-shape particles and spherical particles, were evaluated in terms of cumulative surface area, specific surface area, and pore size distribution.

The simulated initial particle parking structure of cement/geopolymer paste can be used as input to simulate the binder reaction process. As a demonstration to illustrate the influence of particle shape on dissolution, the dissolution of amorphous silica in alkaline solution was simulated. In simulating the dissolution, this study innovatively coupled the Lattice Boltzmann (LB) method and thermodynamics to simulate the physical transport of aqueous ions and the chemical reaction between the amorphous silica and the alkaline solution. The dissolved fractions of amorphous silica at different temperatures were simulated as a function of time, and the simulated results were compared to the experimental measurements. After validation of the simulation model, the influences of continuous stirring, concentration of alkali ions, and particle shape on the dissolution kinetics of silica particles were numerically studied.

2 Materials and Methods

2.1 Materials

The initial particle parking structures of six types of pastes were simulated. These six types were cement paste, slag-based geopolymer paste, fly-ash-based geopolymer paste, binary-blended cement with slag paste, binary-blended cement with fly ash paste, and binary-blended slag with fly-ash-based geopolymer paste. The particle size distributions (PSDs) of cement (type CEM I 42.5N), blast furnace slag (BFS) and fly ash (FA) are plotted in Fig. 1(a). The PSD of cement was obtained from Reference [14], while the PSDs of slag and fly ash were similarly measured by laser diffraction in the lab. The maximum particle sizes of cement, slag, and fly ash are 104 μm, 45 μm, and 47 μm, respectively. The densities of slag and fly ash are 2.97 and 2.33 g/cm^3, respectively, measured by pycnometer in the lab. The density of cement is 3.15 g/cm^3, obtained from Reference [14].

According to Qian et al.[15], the size of models should be at least 2.5 times larger than the largest particle. If taking the maximum particle size of cement as the largest particle in the models, the size of models should be at least 250 μm in each dimension, which leads to rather high computation demand. So this study takes the maximum particle sizes of slag and fly ash as the largest particle size, and hence a predefined cubic container with the dimensions of 125 μm×125 μm×125 μm was used. For cement, the particles were downscaled. The cement particles that corresponded to cumulative mass more than 50 % were removed, and the mass fractions of cement particles corresponded to cumulative mass less than 50 % were multiplied by a factor of 2. In such a way, the maximum particle size of the downscaled cement is 46 μm. The minimum particle size was set at 1 μm, where "size" is further discussed in Section 2.2. The PSDs to be used in simulations are plotted in Fig. 1(b).

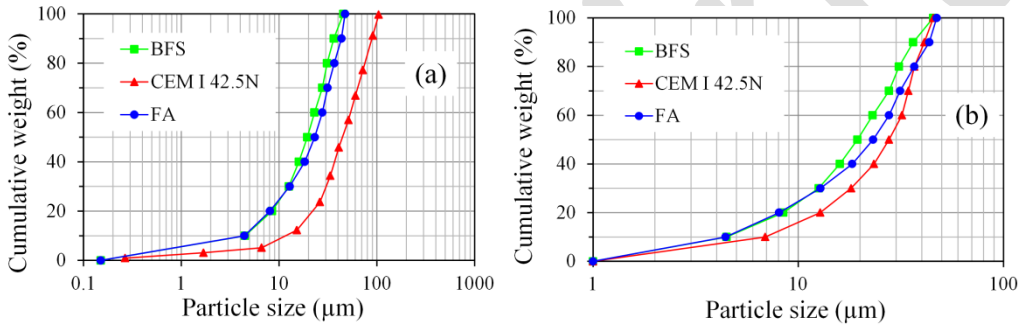

Fig. 1. (a) Experimental PSDs and (b) downscaled PSDs of cement, slag and fly ash

Simulated water with density of 1 g/cm^3 was used to produce the cement-based pastes. A 4 mol/L (sometimes abbreviated as M) sodium hydroxide simulated solution with density of 1.15 g/cm^3 was used to formulate the geopolymer pastes. The mix proportions of cement/geopolymer pastes, given in terms of the mass needed for the predefined cube (125 μm × 125 μm × 125 μm), were tabulated in Table 1. The binder can be cement, slag, or fly ash.

Table 1 Mix proportions of cement/geopolymer pastes given in terms of the mass needed for the predefined cube (125 μm × 125 μm × 125 μm)

Pastes	Binder (×10^{-6}g)	Water(liquid)/binder	Cement/binder	Slag/binder	Fly ash/binder
Cement	2.4803	0.47	1	-	-
BFS	2.2985	0.59	-	1	-
FA	2.1944	0.53	-	-	1
Cement + BFS	2.5259	0.45	0.7	0.3	-
Cement + FA	2.4384	0.45	0.7	-	0.3
BFS + FA	2.4672	0.47	-	0.5	0.5

2.2 Extended Anm material model

The surface of a particle can be represented by a function $r(\theta, \varphi)$ in a 3D spherical polar coordinate system. Once the spherical harmonic coefficients (a_{nm}) are known, the particle shape can be determined according to Eq. (1)

and Eq. (2). $Y_{nm}(\theta, \varphi)$ is the spherical harmonic function with indices n and m ($-n \le m \le n$), $P_{nm}(\cos\theta)$ is the associated Legendre polynomial, and i is the square root of -1 [16].

$$r(\theta,\varphi) = \sum_{n=0}^{\infty} \sum_{m=-n}^{n} a_{nm} Y_{nm}(\theta,\varphi) \quad (1)$$

$$Y_{nm}(\theta,\varphi) = \sqrt{\frac{(2n+1)(n-m)!}{4\pi(n+m)!}} P_{nm}(\cos\theta) e^{im\varphi} \quad (2)$$

The spherical harmonic series requires the particles to be star-shaped. It means that one must not intersect the surface twice when extending any line segment from the center of mass to the surface. The real-shape particles of cement and slag typically satisfy this requirement, while the particles of fly ash do not because of the hollow voids in the fly ash particles. In order to deal with the voids in fly ash particles, first, one can assume no voids, and analyze and park the fly ash particles using the spherical harmonic series, and then remove material digitally to create voids in the fly ash particles before simulating the reaction process. In the current study, the voids were assumed to be evenly distributed in all the parked fly ash particles. For a parked fly ash particle, its volume was apparent volume (V_a) including the volume of voids (V_v) inside the particle. If the apparent density and the real density of fly ash are ρ_a and ρ_r respectively, then there exists the relationship: $V_a\rho_a = (V_a - V_v)\rho_r$, according to which the volume of voids in this parked fly ash particle can be computed. By assuming that the voids exist as a sphere and the spherical coordinates are randomly located inside the fly ash particle, the amount of the material corresponding to the volume of voids can be removed to create the internal voids in the digitization process.

The spherical harmonic coefficients of cement, slag and fly ash were obtained from X-ray computed tomography. Once the spherical harmonic coefficients are known, many geometric properties can be calculated, such as the particle volume, surface area, length, width, and thickness [17]. Length is the longest surface-surface distance in the particle; width is the longest surface-surface distance in the particle such that width is perpendicular to length; and thickness is the longest surface-surface distance in the particle such that thickness is perpendicular to both length and width [17]. Since the particle width is thought to match best with the usual standard experimental sieve classification of particles [18, 19], it was preferentially used for computational sieve analysis [8]. In this study, the particle width was used as the measure of particle size.

In the extended Anm material model, all the particles (either single binder or binary-blended systems) were separated into several sieve ranges according to the particle sizes indicated by the particle widths, and in each sieve range a flag was added to indicate which binder a particle was. The sieve range flag indicates the particle shape database from which the particle shape was chosen while parking the particle into the cubic unit cell. A flag was also added to the parked particle according to which sieve range it was chosen from. In such a way, all parked particles were identified with flags and the initial particle parking structures of binary-blended systems

could be simulated. For all simulations, periodic boundary conditions were employed. Periodic boundary conditions allow a particle to pass through the surface of simulation box and the part outside the simulation box is put on the opposite surface by placing a duplicate particle with the same orientation [9].

2.3 Lattice Boltzmann method

As originated from the lattice gas automata, LB method is considered as a simplified version of molecular dynamics method, utilizing a discrete space, discrete time and discrete velocities [20]. It has been found that the LB method is a powerful method for solving fluid dynamics and ionic transport problems [20-22]. In this study, the LB method was used to simulate the transport of aqueous ions. Usually, a cubic lattice model D3Q19 is used for 3D mass transport simulation. However, the velocity directions may be reduced from 19 (D3Q19) to 7 (D3Q7) without degrading the accuracy when modelling purely diffusive transport without the convective term [23]. For simulating the hydration process of cementitious materials, the transport of aqueous ions is adequately described by being purely diffusive without a convective term. In order to reduce the computational load and improve the simulation efficiency, a cubic lattice model D3Q7 was employed to simulate the ion transport during the dissolution of amorphous silica in an alkaline solution. The evolution of particle distribution functions (not particle size distribution) satisfies the following LB equation [22]:

$$f_i(x + e_i\delta t, t + \delta t) = f_i(x,t) - \frac{\delta t}{\tau}[f_i(x,t) - f_i^{eq}(x,t)] + \omega_i \delta t S \quad (3)$$

where f_i and f_i^{eq} are the non-equilibrium and equilibrium particle distribution function at location x, at time t and in the direction of the velocity i (in this study i = 0, 1, 2, 3, 4, 5, 6), τ is the relaxation time, δt is the time step, e_i is the microscopic velocity at location x, at time t and in velocity direction i, and w_i is the weighting factor in the velocity direction i. S is the source term to consider the influence of dissolution. Without considering the convection term, f_i^{eq} can be calculated using the following equation:

$$f_i^{eq} = \omega_i \sum_{i=0}^{6} f_i(x,t) \quad (4)$$

Fig. 2 displays a flowchart of LB simulation of the dissolution of amorphous silica. After initialization, the simulation starts from calculations of equilibrium particle distribution functions for all lattice nodes according to Eq. (4). Then the amount of dissolved amorphous silica in the current LB time step was calculated to obtain the source terms of ions for each lattice node. The dissolution module will be described in detail in the next section. After calculations of equilibrium particle distribution functions and source terms, the collision process was followed to calculate new non-equilibrium particle distribution functions according to Eq. (3). Then the newly calculated non-equilibrium particle distributions streamed in each direction of velocity. After the streaming process, periodic boundary conditions were applied to calculate the non-equilibrium particle distribution

functions of the lattice nodes on the boundaries of the simulation box. Finally, ion concentrations were updated according to the newly calculated particle distribution functions. If the current time (T) was smaller than the target dissolution period (T_{target}), then the calculation moved to the next iteration; otherwise, the data was output and the program ended.

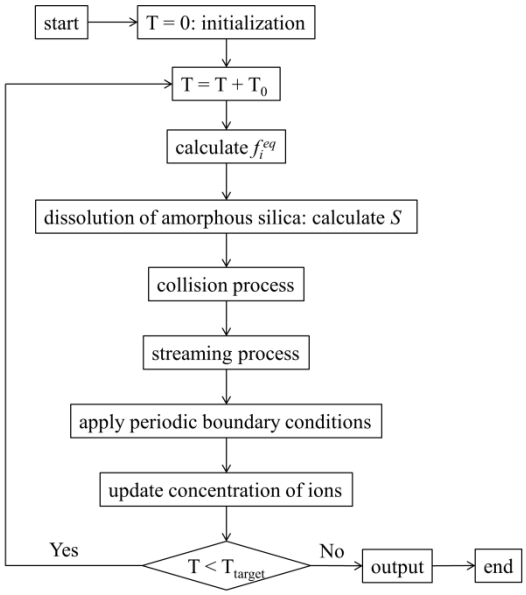

Fig. 2. Flowchart of LB simulation of the dissolution of amorphous silica. T_{target} is the target dissolution period while T is the current dissolution time.

There are three basic physical units involved in the ionic transport in cement-based materials, i.e. length (x_p), time (t_p) and mass (ρ_p), which are different from their corresponding lattice units. For the practical application of LB simulation, conversion was established by dimensional mapping between the lattice units and real physical units: $xL_0 \rightarrow x_p$ (length), $tT_0 \rightarrow t_p$ (time), and $\rho M_0 \rightarrow \rho_p$ (mass), where x, t, and ρ are dimensionless lattice units, and L_0, T_0, and M_0 are conversion factors. With these dimensionless variables (x, t, ρ), the simulation result can be related to any quantities in the physical system. For example, the time mapping T_0 can be obtained from the ion diffusivity D_p (m^2/s) in physical unit and D_{LB} in LB simulation. From the dimensions of diffusivity in LB simulation, we can deduce that $D_p = D_{LB}L_0^2/T_0$. In the lattice models, the lattice diffusivity (D_{LB}) is related to the relaxation time (τ) and the lattice speed (e_s) of sound: $D_{LB} = e_s^2(\tau - \delta t/2)$. In this study, $\tau = 1$ and $e_s^2 = 1/3.5$. So the time factor (T_0) can be calculated:

$$T_0 = \frac{L_0^2 e_s^2 (\tau - \frac{\delta t}{2})}{D_p} \qquad (5)$$

2.4 Dissolution of amorphous silica

The dissolution of amorphous silica ($SiO_2(am)$) in alkaline solution can be described, from the thermodynamic point of view, by the following chemical reaction [24]:

$$SiO_2(am) + 2OH^- \leftrightarrow H_2O + {SiO_3}^{2-} \qquad LogK_{eq} = 2.09 \qquad (6)$$

where K_{eq} is the effective equilibrium constant. By assuming a first-order heterogeneous chemical reaction that the dissolution occurs, one formula, similar to which Kang et al. used for calculating the dissolution rate of carbonates [25], can be obtained to quantify the rate of dissolution (r_D) of amorphous silica:

$$r_D = k_r\left([OH^-] - \left[{SiO_3}^{2-}\right]/K_{eq}\right) \qquad (7)$$

where k_r is the effective forward reaction rate constant (m/s), and [OH^-] and [SiO_3^{2-}] are the concentrations of OH^- and SiO_3^{2-} in the solution (mol/L). However, this equation ignores the influence of chemical activity of the dissolved ions on the dissolution. In order to account for this influence, this study proposed Eq. (8) to determine the rate of dissolution of amorphous silica. The influence of chemical activity of the dissolved ions were taken into account by introducing the term of ion activity product (Q_s) into the dissolution rate equation. a_i is the ion activity of ion i, where i can be SiO_3^{2-}, H_2O or OH^-. Q_s/K_{eq} indicates the degree of saturation with respect to amorphous silica. If $Q_s/K_{eq}<1$, it means undersaturation and indicates more likely that silica dissolves progressively with a larger dissolution rate. If $Q_s/K_{eq}>1$, on the contrary, it means oversaturation and indicates less likely that silica dissolves progressively.

$$r_D = k_r\left([OH^-] - \frac{Q_s}{K_{eq}}\left[{SiO_3}^{2-}\right]\right) \qquad (8)$$

$$Q_s = \frac{{a_{SiO_3}}^{2-} * a_{H_2O}}{{a_{OH^-}}^2} \qquad (9)$$

It is worth noting that there are many other mechanistic models proposed in the literature to describe the dissolution rate [26-30]. But those models are not directly applicable to this study, either due to their complexity with many unknown parameters, or due to their absent consideration of influence of alkalinity on the rate of dissolution. Therefore the empirically established model (Eq. (8)) in this study was used to describe the dissolution rate of amorphous silica in highly alkaline solution in the simulation. Compared to the mechanistic models in the literature, this model is simple for application and a good quality of the simulation results compared to the experimental data (see section 3.4) showed good capability of this model. It is noted that it still needs more data to calibrate this model.

The initial particle parking structure is digitized into digital voxels, so that silica particles will consist of silica voxels (lattice nodes). The dissolution of silica was then simulated by dissolving the silica lattice nodes. Each silica lattice node has six neighbour lattice nodes, so it has six interfaces where dissolution may occur. For each interface of a silica lattice node, the dissolved amount of amorphous silica at one LB time step can be calculated according to Eq. (10). To calculate the rate of dissolution (r_D), the concentrations of [OH^-] and [SiO_3^{2-}], and ion

activity product Q_s were taken from the neighbour lattice node that was in contact with the dissolving interface. By summing up the dissolved amount of amorphous silica on each interface, the total dissolved amount of amorphous silica, also the source term (S) in Eq. (3), can be obtained using Eq. (11).

$$\Delta m = r_D T_0 {L_0}^2 \quad (10)$$

$$\Delta M\ (or\ S) = \sum_{i=1}^{6} r_{D,i} T_0 {L_0}^2 \quad (11)$$

where Δm is the dissolved amount (mol) of amorphous silica on one interface at one LB time step T_0 (s), L_0 (m) is the side length of a lattice node/voxel, ΔM is the total dissolved amount (mol) of amorphous silica at one LB time step T_0, and $r_{D,i}$ is the rate of dissolution of silica on the interface i.

2.5 Influence of temperature

The temperature has a great influence on the diffusion of aqueous ions and the rate of dissolution. Based on the Arrhenius equation, Eq. (12) and Eq. (13) were employed to take into account the influences of temperature on the diffusion coefficients and the rate of dissolution respectively.

$$D_{new} = D_{ref} exp\left[\frac{E_{diff}}{R}\left(\frac{1}{T_{ref}} - \frac{1}{T_{new}}\right)\right] \quad (12)$$

$$r_{D,new} = r_{D,ref} exp\left[\frac{E_a}{R}\left(\frac{1}{T_{ref}} - \frac{1}{T_{new}}\right)\right] \quad (13)$$

where D_{new} and D_{ref} are the diffusion coefficients at the Kelvin temperatures T_{new} and T_{ref}, $r_{D,new}$ and $r_{D,ref}$ are the rates of dissolution at the Kelvin temperatures T_{new} and T_{ref}, R is the gas constant, and E_{diff} and E_a are the activation energy of diffusion and activation energy, respectively.

3 Results and discussion

3.1 Simulated initial particle parking structure of cement/geopolymer paste using spherical particles

Fig. 3 displays the simulated initial particle parking structure of cement/geopolymer paste with single binders of cement, slag, or fly ash. In the images, the colors of red, green, blue, gray and black represent cement, slag, fly ash, water (liquid) and voids in fly ash, respectively. The numbers of particles parked in the simulated initial particle parking structures were 4210, 13515, and 16413 for cement paste, slag-based geopolymer paste, and fly-ash-based geopolymer paste, respectively. The parked particles in the cube were grouped into different sieve ranges according to particle size. In such a way, the cumulative PSD of the particles parked in the cube was obtained. Fig. 4 plots the cumulative PSD of the particles parked in the cube and the target PSD. The simulated PSD is smaller than the target PSD for particles with diameters smaller than 10 μm, and larger than the target PSD for larger particles. The total mass of the particles parked in the cube were 2.4780×10^{-6} g, 2.2983×10^{-6} g, and 2.1944×10^{-6} g, respectively for

cement paste, slag-based geopolymer paste, and fly-ash-based geopolymer paste. The errors of the simulated total masses relative to the target total masses were 0.093 %, 0.008 % and 0.0 %, respectively.

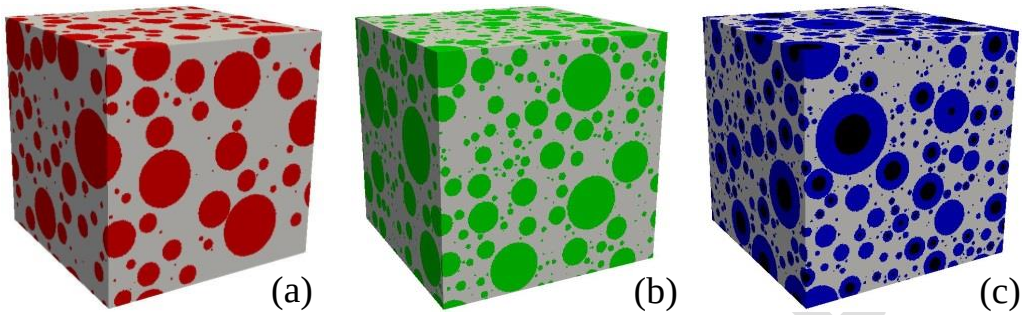

Fig. 3. Digital image of the simulated initial particle parking structure using spherical particles for cement paste (a), slag-based geopolymer paste (b), and fly-ash-based geopolymer paste (c). The size of the cubic unit cell is 125 μm × 125 μm × 125 μm.

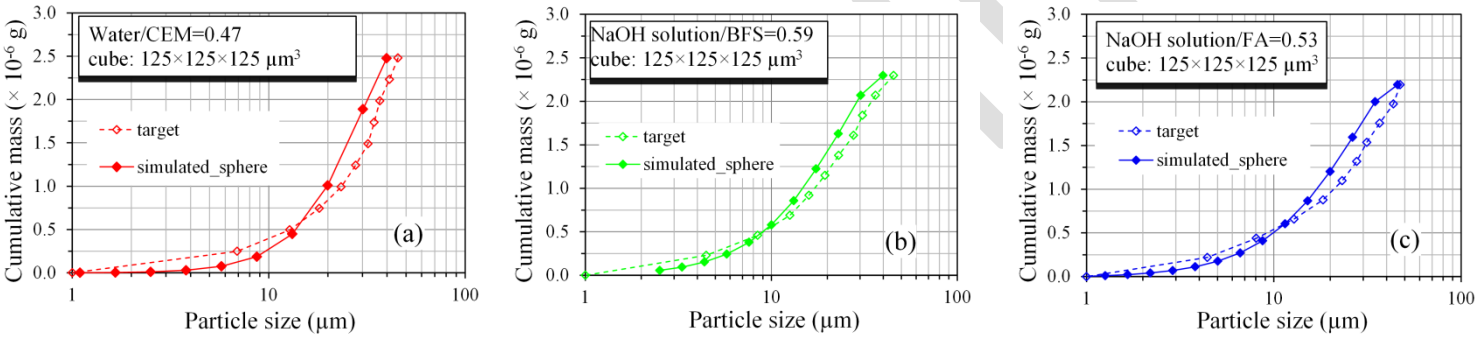

Fig. 4. Simulated and target cumulative PSDs of the particles in the initial particle parking structure for cement paste (a), slag-based geopolymer paste (b), and fly-ash-based geopolymer paste (c).

Fig. 5 shows the simulated initial particle parking structure of binary-blended cement/geopolymer paste using spherical particles. The numbers of the particles parked in the cube were 7466, 8197, and 15744, respectively, for binary-blended cement with slag paste, binary-blended cement with fly ash paste and binary-blended slag with fly-ash-based geopolymer paste. The cumulative PSD of the particles parked in the cube and the target PSD are plotted in Fig. 6. It was found that the simulated cumulative PSD deviates from the target PSD, particularly for particles with diameter larger than 10 μm. The total masses of particles parked in the cube were 2.5258×10^{-6} g, 2.4333×10^{-6} g, and 2.4693×10^{-6} g for binary-blended cement with slag paste, binary-blended cement with fly ash paste and binary-blended slag with fly-ash-based geopolymer paste, respectively. The errors of the simulated total masses relative to the target total masses were 0.004 %, 0.209 %, and 0.085 %, respectively.

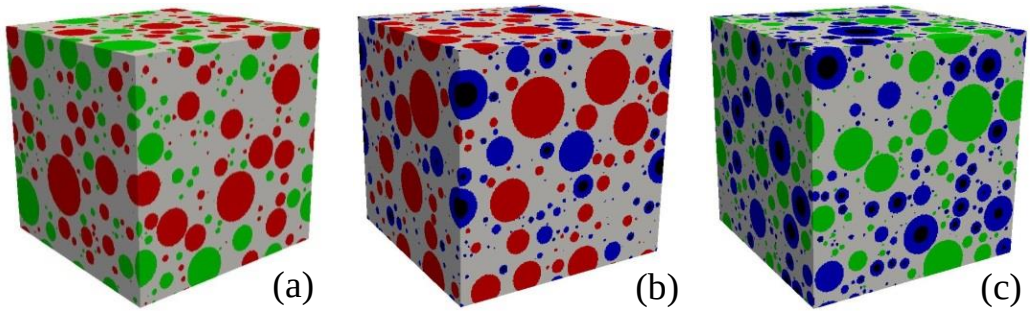

Fig. 5. Digital image of the simulated initial particle parking structure using spherical particles for binary-blended cement with slag paste (a), binary-blended cement with fly ash paste (b), and binary-blended slag with fly-ash-based geopolymer paste (c). The size of the cubic unit cell is 125 μm × 125 μm × 125 μm.

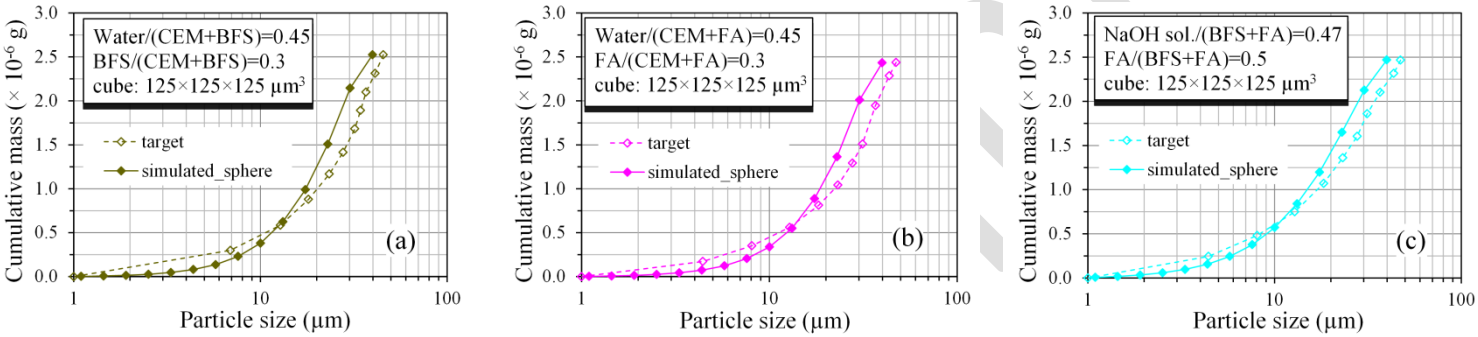

Fig. 6. Simulated and target cumulative PSDs of the particles in the initial particle parking structure using spherical particles for binary-blended cement with slag paste (a), binary-blended cement with fly ash paste (b), and binary-blended slag with fly-ash-based geopolymer paste (c).

3.2 Simulated initial particle parking structure of cement/geopolymer pastes using real-shape particles

In addition to visualization by digital image, the simulated initial particle parking structure by Anm model can be directly visualized using Virtual Reality Modeling Language (VRML). The VRML image displays virtual reality environments of objects, including surface color, image mapped textures, light and reflection mapping, and transparency [31]. Fig. 7 displays the simulated initial particle parking structure of the single binder pastes as VRML and digital images. Because the periodic boundary conditions allow a particle to pass through the surface of simulation box, therefore, there were particles sticking out beyond the simulation box in the VRML images. In the digitization process, all the parts outside the simulation box were removed, so there were no particles sticking out beyond the simulation box in the digital images. The numbers of particles parked in the simulated initial particle parking structure were 2454, 8558, and 9154, respectively, for cement paste, slag-based geopolymer paste and fly-ash-based geopolymer paste.

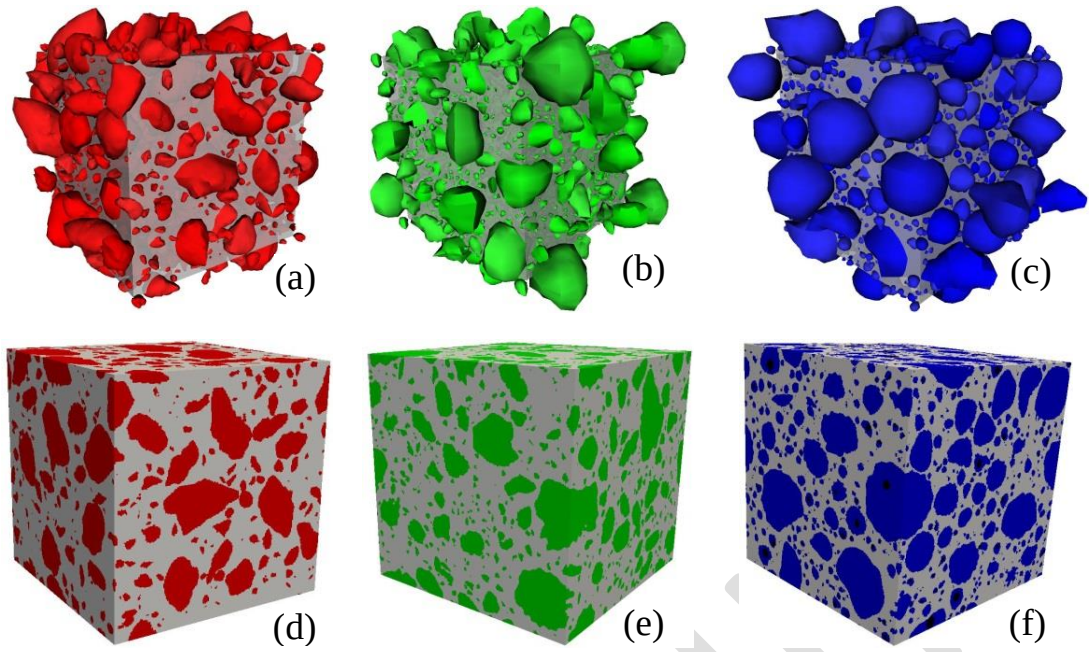

Fig. 7. VRML (a, b, c) and digital (d, e, f) images of the simulated initial particle parking structure using real-shape particles for cement paste (a, d), slag-based geopolymer paste (b, e), and fly-ash-based geopolymer paste (c, f). The size of the cubic unit cell is 125 μm × 125 μm × 125 μm.

The cumulative PSD of the particles parked in the cube and the target PSD are plotted in Fig. 8. Compared to the simulated PSDs of slag-based geopolymer paste, the simulated PSDs of cement paste and fly-ash-based geopolymer paste agree very well with their target ones. The total masses of particles parked in the initial particle parking structures were 2.4885×10^{-6} g, 2.2906×10^{-6} g, and 2.1965×10^{-6} g for the cement paste, slag-based geopolymer paste and fly-ash-based geopolymer paste, respectively. The errors of the simulated total masses relative to the target total amounts were 0.331%, 0.344 %, and 0.096 %, respectively.

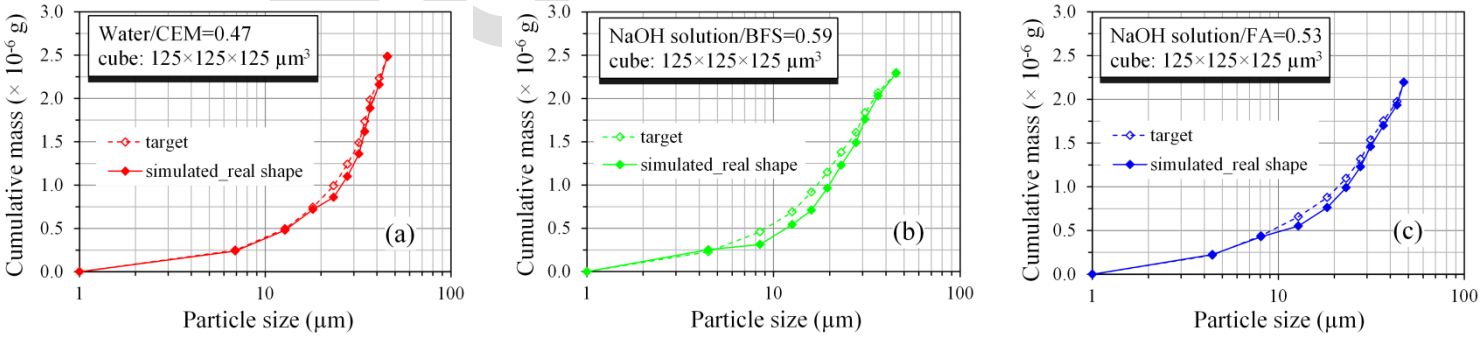

Fig. 8. Simulated and target cumulative PSDs of the particles in the initial particle parking structure using real-shape particles for cement paste (a), slag-based geopolymer paste (b), and fly-ash-based geopolymer paste (c).

The simulated initial particle parking structures of binary-blended cement/geopolymer pastes are shown as VRML and digital images in Fig. 9. The numbers of particles parked in the simulated initial particle parking structures were 9006, 4383, and 9342 for cement blended with slag, cement blended with fly ash and slag blended with fly-ash-based

geopolymer paste, respectively. The cumulative PSDs for particles parked in the simulated initial particle parking structures and the target PSDs are plotted in Fig. 10. The simulated PSDs of binary-blended cement/geopolymer pastes agree well with their respective target. The total amounts of particles parked in the binary-blended initial particle parking structures were 2.5244×10^{-6} g, 2.4158×10^{-6} g, and 2.4609×10^{-6} g, respectively for cement blended with slag, cement blended with fly ash and slag blended with fly-ash-based geopolymer paste. The errors of simulated total masses relative to the target total masses were 0.059 %, 0.927 %, and 0.255 %, respectively.

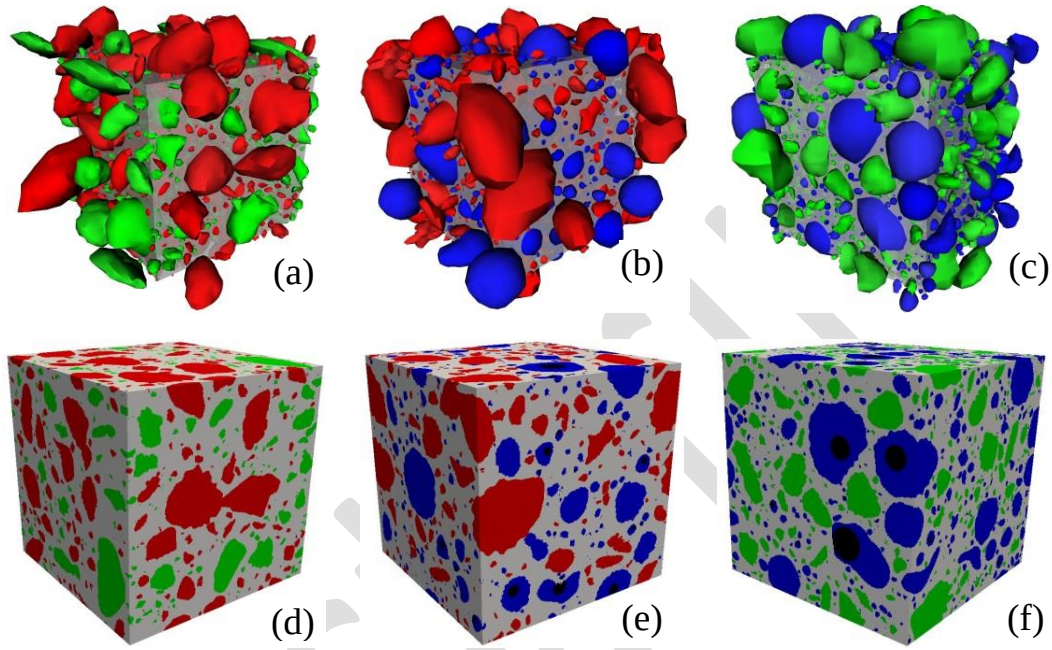

Fig. 9. VRML (a, b, c) and digital (d, e, f) images of the simulated initial particle parking structure using real-shape particles for binary-blended cement with slag paste (a, d), binary-blended cement with fly ash paste (b, e), and binary-blended slag with fly-ash-based geopolymer paste (c, f). The size of the cubic unit cell is 125 μm × 125 μm × 125 μm.

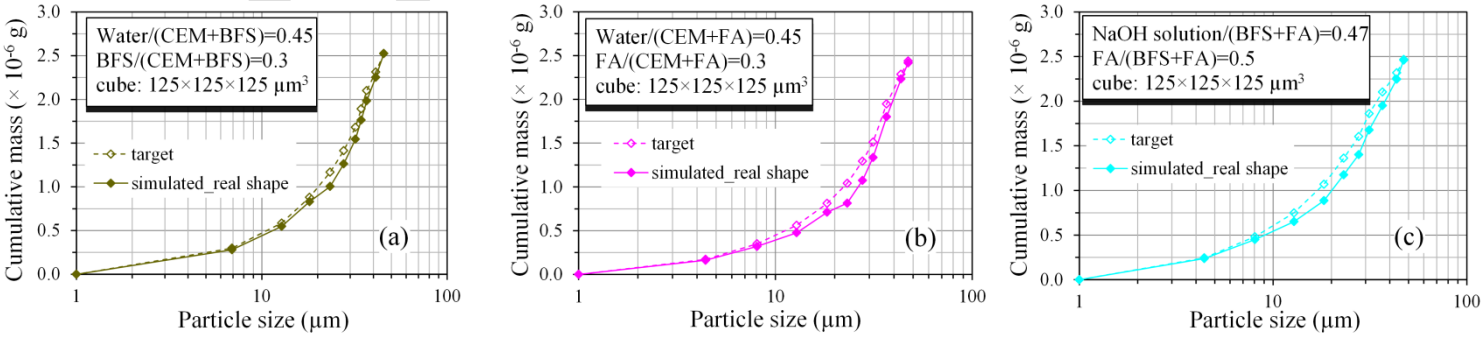

Fig. 10. Simulated and target cumulative PSDs of the particles in the initial particle parking structure using real-shape particles for binary-blended cement with slag paste (a), binary-blended cement with fly ash paste (b), and binary-blended slag with fly-ash-based geopolymer paste (c).

3.3 Evaluation of the simulated initial particle parking structure

Previous simulation results suggested that the additional specific surface area (surface/volume) of real-shape particles relative to spherical particles accelerates hydration of cement [7], and also influences the microstructure formation of cement paste [7, 12]. The pore structure of a hydrated cement paste has a great impact on its diffusive properties [32, 33], which further influences its resistance to environmental aggressive ingredients such as chloride and sulfate ions. With these in mind, the simulated initial particle parking structures, using spherical particles and real-shape particles, were evaluated in terms of cumulative surface area and specific surface area (particle surface area/particle volume, μm^{-1}) of the parked particles, and pore size distribution.

Fig.11 shows the cumulative surface area and specific surface area of the parked particles as a function of particle size for the simulated initial particle structures of cement/geopolymer pastes with single binder of cement, slag, or fly ash. The cumulative surface areas of parked particles using real-shape particles and spherical particles are close to each other at large particle sizes. However, the cumulative surface area of the parked particles using real-shape particles is much larger at small particle sizes, compared to using spherical particles. This is because the real-shape particles at small particle sizes have much larger specific surface areas, which is to be discussed in the following paragraph. The total surface areas of the parked particles using real-shape particles were 3.615×10^5 μm^2, 5.053×10^5 μm^2, and 5.284×10^5 μm^2, respectively, for cement paste, slag-based geopolymer paste and fly-ash-based geopolymer paste. By using spherical particles, the total surface areas of the parked particles were 2.631×10^5 μm^2, 4.083×10^5 μm^2, and 4.705×10^5 μm^2, respectively. The total surface areas of the parked particles using real-shape particles were 37.40 %, 23.76 %, and 12.31 % larger respectively than those using spherical particles.

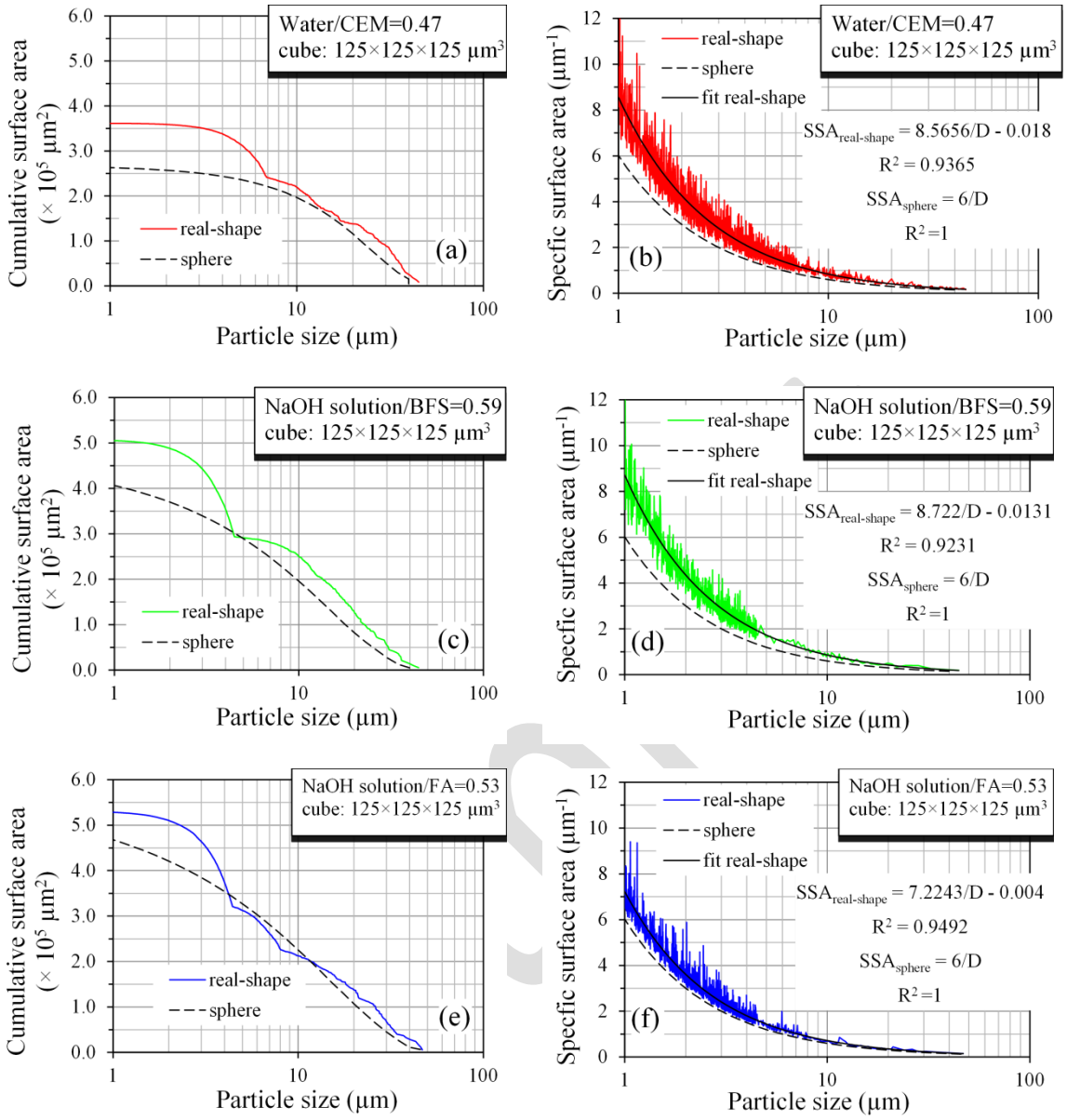

Fig. 11. Cumulative surface area (a, c, e) and specific surface area (b, d, f) of the parked particles in the simulated initial particle parking structure for cement paste (a, b), slag-based geopolymer paste (c, d), and fly-ash-based geopolymer paste (e, f).

The specific surface areas of the parked particles using real-shape particles were larger, particularly at small particle sizes, than those using spherical particles. A decreasing trend of specific surface area can be observed as a function of particle size. The fitted relationship of specific surface area as a function of particle size for the parked real-shape particles also suggested a great dependence of specific surface area on particle size. The particle shape also has a significant influence on the specific surface area of the parked real-shape particles, resulting in large variations of specific surface area. For this reason, a particle with larger particle size may have larger specific surface area than a particle with smaller particle size, as opposed to the decreasing trend. For a spherical particle with diameter *D*, its

specific surface area is 6/*D*. It can be seen that the specific surface area of a spherical particle only depends on the particle diameter. Therefore, the specific surface area of the parked spherical particles has the same distribution as a function of particle size/diameter for all the simulated initial particle parking structures using spherical particles. Whether using real-shape particles or using spherical particles, a relationship exists between specific surface area (*SSA*) and particle size (*D*): $SSA = F/D$, where *F* is a pre-factor. Compared to the relationship for the parked spherical particles, the relationship for the parked real-shape particles has a pre-factor with 42.76 %, 45.37 % and 20.41 % larger for cement paste, slag-based geopolymer paste and fly-ash-based geopolymer paste, respectively. A larger pre-factor results in a larger specific surface area.

Cement finesses (Blaine, m^2/kg) significantly influenced hydration process and early-age properties of cement-based materials [12, 34, 35]. Since the specific surface areas of individual particles cannot explicitly reflect the binder fineness, the bulk specific surface area was defined as the ratio of the total surface area of the parked particles divided by the total volume of the parked particles. A larger bulk specific surface area leads to a larger binder fineness. The bulk specific surface areas of the parked particles using real-shape particles were 0.4576 μm^{-1}, 0.6552 μm^{-1}, and 0.5606 μm^{-1}, respectively for cement paste, slag-based geopolymer paste, and fly-ash-based geopolymer paste. By using spherical particles, the bulk specific surface areas were 0.3344 μm^{-1}, 0.5277 μm^{-1}, and 0.4996 μm^{-1}, respectively. Compared to those of the parked particles using spherical particles, the bulk specific surface areas of the parked particles using real-shape particles were 36.84 %, 24.16 %, and 12.21 % larger, respectively.

In Fig. 12, the columns display the cumulative surface area and specific surface area of the parked particles for binary-blended cement/geopolymer paste. The cumulative surface areas of the parked real-shape particles and spherical particles are close to each other at larger particle sizes, while at smaller particle sizes the cumulative surface area of the parked real-shape particles is much larger. This can also be attributed to the larger specific surface areas of real-shape particles at smaller particle sizes. The total surface areas of the parked particles using real-shape particles were 4.286×10^5 μm^2, 4.081×10^5 μm^2, and 5.669×10^5 μm^2, respectively for binary-blended cement with slag paste, binary-blended cement with fly ash paste and binary-blended slag with fly-ash-based geopolymer paste. By using spherical particles, the total surface areas of the parked particles were 3.298×10^5 μm^2, 3.402×10^5 μm^2, and 4.746×10^5 μm^2, respectively. The total surface areas of the parked particles using real-shape particles were 29.96 %, 19.96 %, and 19.45 % larger, respectively, than those of the spherical particles.

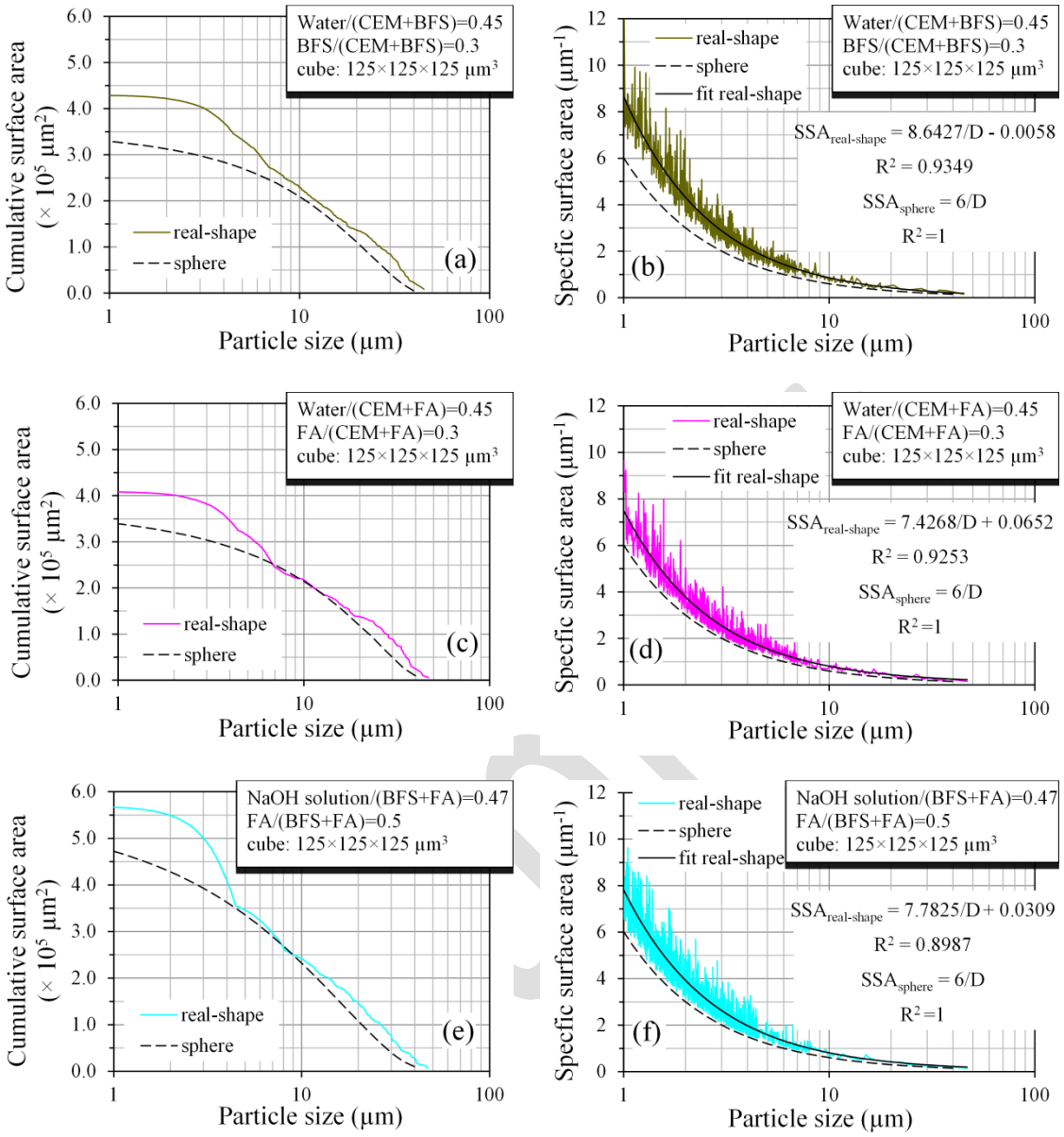

Fig. 12. Cumulative surface area (a, c, e) and specific surface area (b, d, f) of the parked particles in the simulated initial particle parking structure using real-shape particles for binary-blended cement with slag paste (a, b), binary-blended cement with fly ash paste (c, d), and binary-blended slag with fly-ash-based geopolymer paste (e, f).

For all binary-blended cement/geopolymer pastes, it can also be seen that the specific surface areas of the parked particles using real shape particles were always larger than those of the parked spherical particles. Compared to the relationship for the parked spherical particles, the relationship for the parked real-shape particles has a pre-factor (F) with 44.04 %, 23.68 % and 29.71 % larger for binary-blended cement with slag paste, binary-blended cement with fly ash paste and binary-blended slag with fly-ash-based geopolymer paste, respectively. The bulk specific surface areas of the parked particles using real-shape particles were 0.5245 μm^{-1}, 0.4758 μm^{-1}, and 0.6011 μm^{-1}, respectively, for binary-blended cement with slag paste, binary-blended cement with fly ash paste and binary-

blended slag with fly-ash-based geopolymer paste. By using spherical particles, the bulk specific surface areas were 0.4040 μm^{-1}, 0.3956 μm^{-1}, and 0.5043 μm^{-1}, respectively. Compared to those of the parked particles using spherical particles, the bulk specific surface areas of the parked particles using real-shape particles were 29.83 %, 20.27 %, and 19.19 % larger, respectively.

Yang et al. developed an image-based algorithm to obtain the pore size distribution of porous media in 2D [36]. The current study extended this algorithm from 2D to 3D to calculate the pore size distribution of the digitized initial particle parking structure. The vacant space after parking binder particles was considered as pores in the simulated microstructure. Fig. 13 presents the pore size distributions of the simulated initial particle parking structure at digitization resolutions of 1, 0.5 and 0.25 μm per cubic voxel edge for cement paste. Regardless of using real-shape particles or using spherical particles, the simulated initial particle parking structure has a finer pore size distribution when it is digitized with a higher resolution. At all digitation resolutions, the simulated initial particle parking structure using real-shape particles has a slightly finer pore size distribution than that using spherical particles.

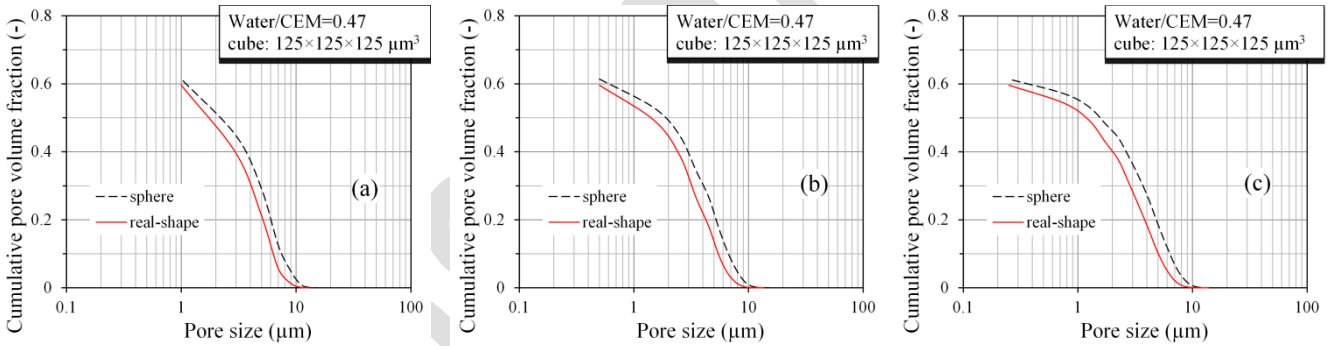

Fig. 13. Pore size distribution of the simulated initial particle parking structure digitized at different resolutions: (a) 1 μm^3/voxel, (b) 0.5 μm^3/voxel, (c) 0.25 μm^3/voxel.

Figs. 14 and 15 present the pore size distributions of the simulated initial particle parking structures for neat and binary-blended cement/geopolymer paste, respectively. All the simulated initial particle parking structures were digitized with a resolution of 0.5 μm per cubic voxel edge. It can be seen that the pore size distributions of the simulated initial particle parking structures using real-shape particles and spherical particles are very close to each other. In general, the pore size distributions of the simulated initial parking structures using real-shape particles shift slightly to small pores when compared to those using spherical particles. From the comparisons, it can be concluded that particle shape does not significantly influence the pore size distribution of the simulated initial particle parking structure.

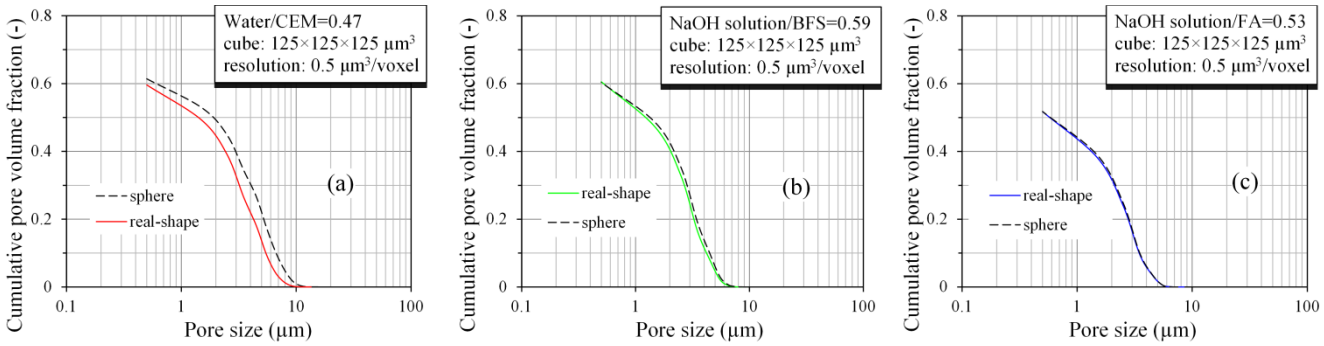

1 **Fig. 14.** Pore size distribution of the simulated initial particle parking structure for cement paste (a), slag-based
2 geopolymer paste (b), and fly-ash-based geopolymer paste (c).

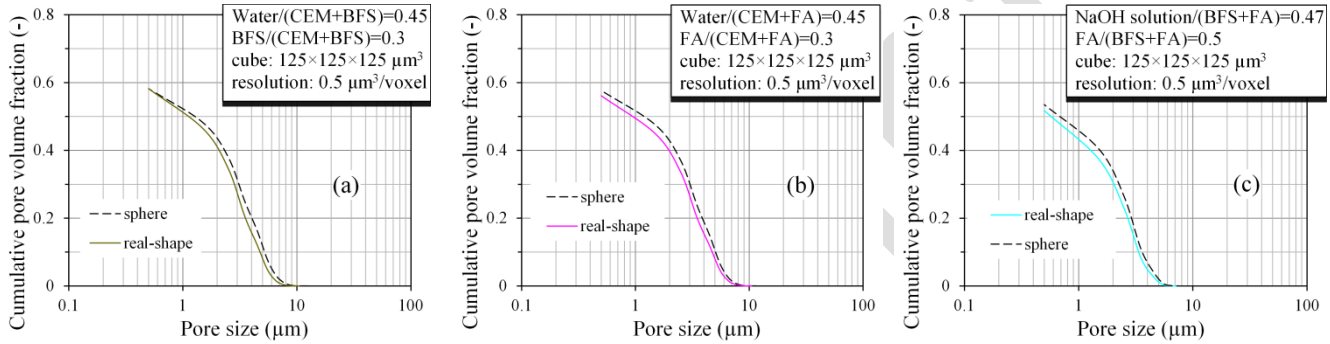

3 **Fig. 15.** Pore size distribution of the simulated initial particle parking structure for binary-blended cement with slag
4 paste (a), binary-blended cement with fly ash paste (b), and binary-blended slag with fly-ash-based geopolymer paste
5 (c).

6 3.4 Numerical simulation of the dissolution of amorphous silica in alkaline solution

7 Niibori et al. experimentally studied the rates of dissolution of four types of amorphous silica in 0.1 mol/L
8 NaOH solution [37]. Wako-gel LC-50H silica is one of the four types of amorphous silica and its particle
9 diameter was fixed at 50 μm. In our study the dissolution of Wako-gel LC-50H silica was simulated.
10 According to the photomicrographs of amorphous silica, it can be seen that the silica particles had very
11 similar particle shapes to those of slag particles. So the database of spherical harmonic coefficients of slag
12 particles was used as the particle shape database to generate the initial particle parking structure of amorphous
13 silica in alkaline solution.

14 In the experiments, Niibori et al. dissolved 100 mg of amorphous silica in 500 mL of NaOH solution with
15 continuous stirring and no obvious signs of precipitation or gel formation. In the simulation, 1.4×10^{-7} g of
16 silica with diameter of 50 μm was parked in a cube of 1000 μm × 1000 μm × 1000 μm to obtain the initial particle
17 parking structure. This amount of silica is equivalent to 70 mg of silica placed in a volume of 500 mL. Since 70
18 mg is less than 100 mg, there will be no precipitation or gel formation needing to be simulated in the model

systems. The simulated initial particle parking structure was then digitized with a resolution of 10 μm × 10 μm × 10 μm per voxel. For all the simulations of the dissolution of amorphous silica in this study, the LB method was used to compute the transport of the aqueous ions (as described in section 2.3), and the proposed dissolution model was used to calculate the dissolved amount of amorphous silica in each LB time step (as described in section 2.4). In order to take into account the effect of continuous stirring on the dissolution of amorphous silica in the simulation, the dissolved SiO_3^{2-} ions at each LB step were evenly distributed as source terms into the solution lattice nodes. The rate constant (k_r) was obtained as 8.3×10^{-8} m/s by parameter study, and the activation energy (E_a) was selected to be 8.3×10^4 J/mol out of the reported range of 7.7 to 8.8 $\times10^4$ J/mol [37]. The values of the diffusion coefficients and the activation energy of diffusion of aqueous ions are presented in Table 2.

Table 2 Diffusion coefficients and activation energy of diffusion of aqueous ions

	Na^+	OH^-	SiO_3^{2-}	reference
D_{ref} (25°C, $\times10^9$ m^2/s)	1.33	5.28	0.70	[38, 39]
E_{diff} ($\times10^4$ J/mol)	1.67	1.80	2.46	calculated [40, 41]

Fig. 16 shows the dissolved fraction of amorphous silica in 0.1 mol/L NaOH solution at different temperatures by simulations and experiments. It can be seen that the dissolved fractions of amorphous silica at different temperatures by simulations agree very well with the experimental results. This indicates the simulation using the real-shape particles can capture the dissolution kinetics of amorphous silica in alkaline solution. In addition to the dissolution kinetics, the simulation can also output the aqueous phase composition of the solution. For instance, the simulation concentrations of OH^- ($[OH^-]$) and Si ([Si]) as a function of time are plotted in Fig. 17. The simulation concentration was calculated as the average of concentrations in liquid lattice nodes. Higher temperature accelerates the dissolution of amorphous silica, which therefore results in a more rapid decrease of $[OH^-]$ and increase of [Si] when the temperature increases. At the dissolved fraction of 1, the simulated $[OH^-]$ and [Si] were 0.0954 mol/L and 0.0023 mol/L, respectively. These results are consistent with the results calculated according to Eq. (6).

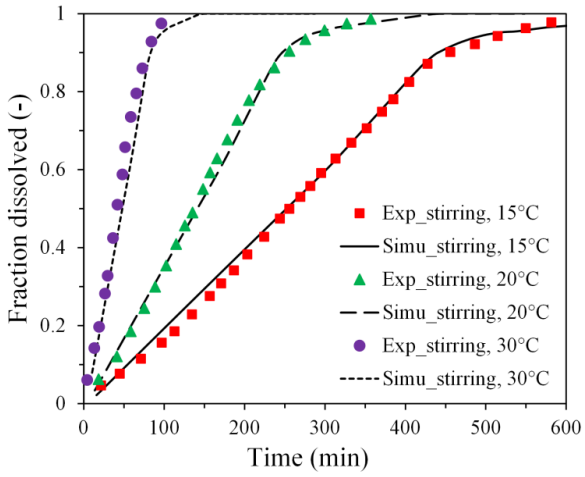

Fig. 16. Fraction dissolved of amorphous silica in 0.1 M NaOH solution by simulations and experiments

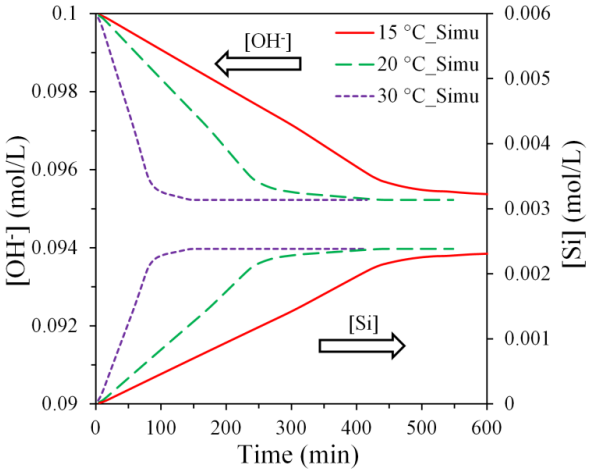

Fig. 17. Simulated concentrations of OH^- and Si as a function of time

After validation by the experimental results, the model were extended to study the influences of initial alkali ion concentration, particle shape, and continuous stirring on the dissolution kinetics of amorphous silica in alkaline solution. In this study, three NaOH solutions with concentrations of 0.05 mol/L, 0.1 mol/L, and 0.2 mol/L were used to study the influence of alkali concentration on the dissolution kinetics of amorphous silica at 20 °C. In order to study the influence of particle shape on the dissolution kinetics of amorphous silica, two types of real-shape particles were used (shapeNo179 and shapeNo89) and compared to the spherical particle. In these three simulated initial particle parking structures, one particle with volume of about 50 000 μm^3 was parked in a cube of 100 μm × 100 μm × 100 μm and the simulation concentration of alkali and temperature were 0.1 mol/L and 20 °C, respectively. The simulated initial particle parking structures were digitized with a resolution of 1 μm per cubic voxel edge. Table 3 lists the parameters of these three types of particles parked in the initial particle parking structure and presents the particle shape as a digital/VRML image.

Table 3 Parameters of the particle parked and the particle shape as a digital/VRML image

Particle shape	Parameters	Value	Particle shape as a digital/VRML image
sphere	Diameter (μm)	45.7154	
	Surface area (μm^2)	6562.28	
	Volume (μm^3)	49999.5	
	Specific surface area (/μm)	0.1312	
shapeNo179	Width (μm)	56.4119	
	Surface area (μm^2)	8162.54	
	Volume (μm^3)	50000.0	
	Specific surface area (/μm)	0.1633	
shapeNo89	Width (μm)	61.1097	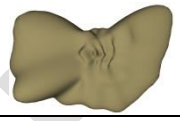
	Surface area (μm^2)	9978.84	
	Volume (μm^3)	49999.9	
	Specific surface area (/μm)	0.1996	

Fig. 18(a) shows the dissolved fraction of amorphous silica in NaOH solution with different concentrations of alkali. The dissolved fraction of amorphous silica increases more rapidly as the concentration of alkali increases. A higher alkali concentration leads to a higher alkalinity and the higher alkalinity accelerates the removal of Si tetrahedras from the amorphous silica. So the rate of dissolution increases with the increase of alkali concentration. This simulation further validates that the determination of dissolution rate using a thermodynamic method (Eq. (8)) is capable of considering the influence of alkali concentration on the dissolution kinetics. It can be seen in Table 3 that the sphere, shapeNo179 and shapeNo89 particles have nearly the same volume, while the shapeNo89 particle has the largest surface area and the spherical particle has the smallest surface area, which can also be visually observed from the digital/VRML images. Fig. 18(b) plots the dissolved fraction of amorphous silica as a function of time for these three types of particle shape. Through the whole dissolution process, the shapeNo89 particle always has the largest dissolved fraction of amorphous silica, while the sphere particle always has the smallest dissolved fraction of amorphous silica. This illustrates that the particle shape has a great influence on the dissolution kinetics, which confirms the findings in the literature [4, 5]. The particle with larger specific surface dissolves faster than the particle with smaller specific surface area.

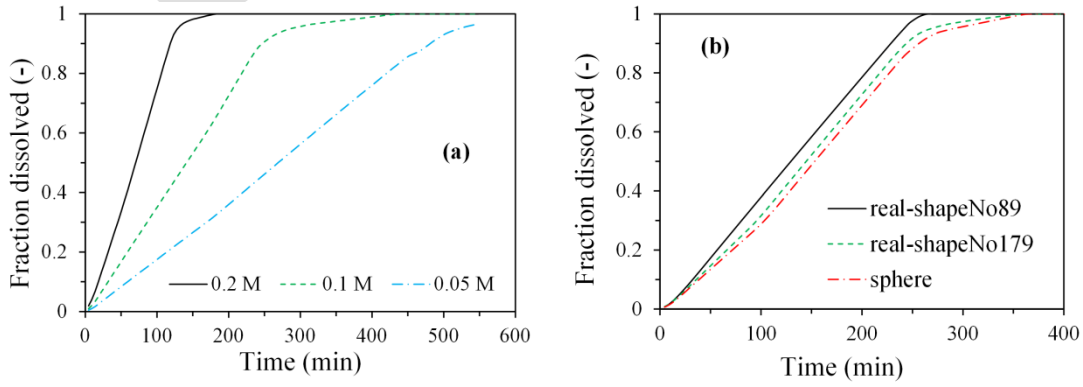

Fig. 18. Influences of the alkali concentration (a) and the particle shape (b) on the dissolution kinetics

In experimental measurements, continuous stirring was used to make an even distribution of silica particles in alkaline solution and avoid particle aggregation. However, these measurements cannot then reflect the real dissolution kinetics of amorphous silica in alkaline solution. In order to study the effect of continuous stirring on the dissolution kinetics of amorphous silica in alkaline solution at different temperatures, the condition of even distribution of SiO_3^{2-} ions once they were dissolved in each LB step was not applied in the simulation. Fig. 19 shows the dissolved fraction of amorphous silica by simulation without stirring in comparison with the experimental measurements with continuous stirring. The dissolved fraction of amorphous silica in simulations without stirring was always smaller than that with continuous stirring in experiments. To reach a dissolved fraction of 0.2, it takes 6.95, 4.18, and 1.72 hours respectively for amorphous silica in alkaline solution without continuous stirring at 15 °C, 20 °C and 30 °C, while it only needs 1.99, 1.07, and 0.32 hours, respectively, for amorphous silica in alkaline solution with continuous stirring. These figures show that the dissolution of amorphous silica in alkaline solution is accelerated 2.49, 2.91, and 4.38 times faster by the continuous stirring at 15 °C, 20 °C and 30 °C, respectively. It can be seen that continuous stirring has a great acceleration influence on the dissolution kinetics of amorphous silica in alkaline solution.

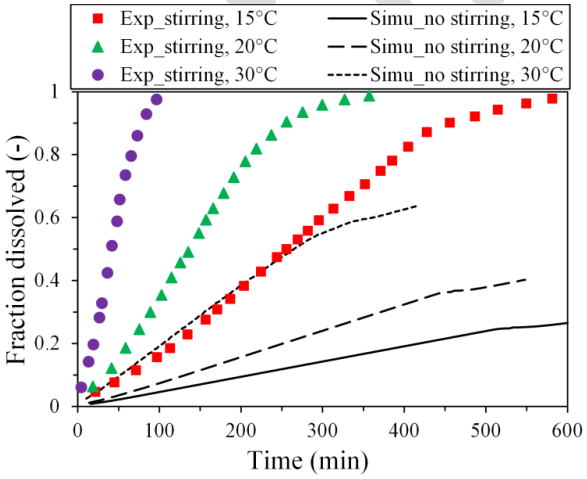

Fig. 19. Fraction dissolved of amorphous silica in 0.1 M NaOH solution by simulations without continuous stirring

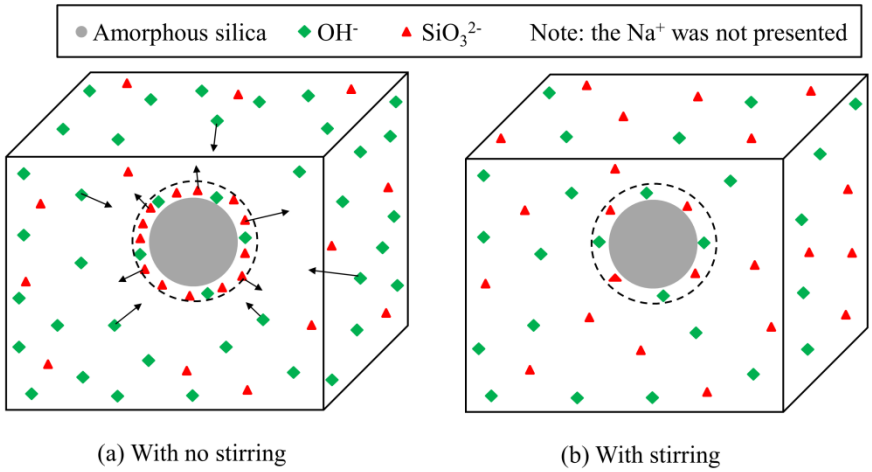

Fig. 20. Schematic illustration of the effect of continuous stirring on the dissolution of amorphous silica. For a clear representation, Na^+ was not represented in the graphs.

As schematically illustrated in Fig. 20(a), the concentration of SiO_3^{2-} near the surface of silica increases while the concentration of OH^- near the surface of silica becomes decreased with the dissolution of silica. Continuous stirring accelerates the diffusion of the dissolved SiO_3^{2-} ions away from the silica surface while accelerates the diffusion of OH^- ions to the silica surface. Therefore, there are lower concentration of SiO_3^{2-} and higher concentration of OH^- near the surface of silica for the system with stirring when compared to the system with no stirring (see Fig. 20(b)). According to Eq. (6), from the thermodynamic point of view, lower concentration of SiO_3^{2-} and higher concentration of OH^- make the thermodynamic equilibrium move to the right, and hence favors the dissolution of silica. This thermodynamic characteristic was explicitly simulated by Eq. (8). Additionally, lower concentration of SiO_3^{2-} results in lower activity of SiO_3^{2-} and higher concentration of OH^- leads to higher activity of OH^-. As a result, the ion activity product becomes decreased (Eq. (9)), which results in a larger dissolution rate (Eq. (8)). Therefore, continuous stirring accelerated the dissolution of amorphous silica and it was explicitly simulated by the simulation.

4 Conclusions

By implementing the spherical harmonic series method to characterize particle shape, this study simulated the initial particle parking structures of neat and binary-blended cement/geopolymer pastes using real-shape particles of cement, slag, or fly ash. The cumulative PSDs of the particles parked in each sieve range and the total mass agreed well with the target values. Compared to the simulated initial particle structures using spherical particles, the simulated initial particle structures using real-shape particles have total surface areas with up to 37.40 % larger. Regardless of the type of paste, the bulk specific surface area of the parked particles using real-shape particles was at least 12.21 % larger than that using spherical particles. The pore size distributions of the

simulated initial particle structures, using real-shape or spherical shape particles, were not significantly influenced by particle shape.

As a demonstration to illustrate the influence of particle shape on dissolution, the dissolution of amorphous silica in alkaline solution was simulated based on real-shape particles by coupling LB method and thermodynamics. The dissolved silica fractions at different temperatures in the simulations agreed well with the experimental measurements. The simulations of the dissolution of amorphous silica in NaOH solution with different concentrations of alkali show that the dissolved silica fraction increases with the increase of alkali concentration. These simulation results further validated the numerical model that a higher alkali concentration leaded to a higher alkalinity and the higher alkalinity accelerates the removal of Si tetrahedras from amorphous silica. The simulation results also show that the particle with larger specific surface area dissolves faster than the particle with smaller specific surface area, and that continuous stirring accelerates dissolution of amorphous silica several times faster in alkaline solution as opposed to no stirring.

Acknowledgements

The authors thank Mr. Peng Gao for helping with calculations using HYMOSTRUC3D, and the first author would like to thank the China Scholarship Council (Grant Number 201406160086) for financial support in his PhD study.

Conflict of interest

References

[1] H.M. Jennings, S.K. Johnson, Simulation of microstructure development during the hydration of a cement compound, J. Am. Ceram. Soc. 69(11) (1986) 790-795.

[2] P. Navi, C. Pignat, Three-dimensional characterization of the pore structure of a simulated cement paste, Cem. Concr. Res. 29(4) (1999) 507-514.

[3] K. Maekawa, R. Chaube, T. Kishi, Modeling of concrete performance: hydration, microstructure formation and mass transport, E and FN SPON, London (1999)

[4] K.v. Breugel, Simulation of hydration and formation of structure in hardening cement-based materials, PhD thesis, Delft University of Technology, Delft, 1991.

[5] G. Pólya, G. Szegő, Isoperimetric inequalities in mathematical physics, Princeton University Press, 1951.

[6] H.F. Taylor, Cement chemistry, Thomas Telford, 1997.

[7] J.W. Bullard, E.J. Garboczi, A model investigation of the influence of particle shape on portland cement hydration, Cem. Concr. Res. 36(6) (2006) 1007-1015.

[8] E.J. Garboczi, Three-dimensional mathematical analysis of particle shape using X-ray tomography and spherical harmonics: Application to aggregates used in concrete, Cem. Concr. Res. 32(10) (2002) 1621-1638.

[9] Z. Qian, E. Garboczi, G. Ye, E. Schlangen, Anm: a geometrical model for the composite structure of mortar and concrete using real-shape particles, Mater. Struct. 49(1-2) (2016) 149-158.

[10] D.W. Cooper, Parking problem (sequential packing) simulations in two and three dimensions, Journal of Colloid and Interface Science 119(2) (1987) 442-450.

[11] S. Thomas, Y. Lu, E. Garboczi, Improved Model for Three-Dimensional Virtual Concrete: Anm Model, Journal of Computing in Civil Engineering 30(2) (2015) 04015027.

[12] G. Ye, Experimental Study and Numerical Simulation of the Development of the Microstructure and Permeability of Cementitious Materials, PhD thesis, Delft University of Technology, 2003.

[13] P. Gao, G. Ye, J. Wei, Q. Yu, Simulation of the development of pH in the pore solution of slag cement paste at early age, RILEM International Symposium on Concrete Modelling, , Beijing, China, 2014, pp. 273-280.

[14] X. Ouyang, G. Ye, K. van Breugel, Experimental and numerical evaluation of mechanical properties of interface between filler and hydration products, Constr. Build. Mater. 135 (2017) 538-549.

[15] Z. Qian, E. Schlangen, G. Ye, K. van Breugel, Modeling Framework for Fracture in Multiscale Cement-Based Material Structures, Materials 10(6) (2017) 587.

[16] G. Arfken, Mathematical Methods for Physicists, 2nd Academic Press, New York, 1970.

[17] M.A. Taylor, E.J. Garboczi, S. Erdogan, D. Fowler, Some properties of irregular 3-D particles, Powder Technol. 162(1) (2006) 1-15.

[18] S. Erdoğan, E.J. Garboczi, D. Fowler, Shape and size of microfine aggregates: X-ray microcomputed tomography vs. laser diffraction, Powder Technol. 177(2) (2007) 53-63.

[19] J.M. Fernlund, The effect of particle form on sieve analysis: a test by image analysis, Engineering Geology 50(1) (1998) 111-124.

[20] M. Zhang, Multiscale lattice Boltzmann-finite element modelling of transport properties in cement-based materials, PhD thesis, Delft University of Technology, Delft, 2013.

[21] M. Zhang, G. Ye, K. van Breugel, Modeling of ionic diffusivity in non-saturated cement-based materials using lattice Boltzmann method, Cem. Concr. Res. 42(11) (2012) 1524-1533.

[22] A.A. Mohamad, Lattice Boltzmann method: fundamentals and engineering applications with computer codes, Springer Science & Business Media, , 2011.

[23] N. Jeong, D.H. Choi, C.-L. Lin, Estimation of thermal and mass diffusivity in a porous medium of complex structure using a lattice Boltzmann method, International Journal of Heat and Mass Transfer 51(15) (2008) 3913-3923.

[24] B. Lothenbach, F. Winnefeld, Thermodynamic modelling of the hydration of Portland cement, Cem. Concr. Res. 36(2) (2006) 209-226.

[25] Q. Kang, D. Zhang, S. Chen, X. He, Lattice Boltzmann simulation of chemical dissolution in porous media, Physical Review E 65(3) (2002) 036318.

[26] E.H. Oelkers, S.R. Gislason, The mechanism, rates and consequences of basaltic glass dissolution: I. An experimental study of the dissolution rates of basaltic glass as a function of aqueous Al, Si and oxalic acid concentration at 25 C and pH= 3 and 11, Geochim. Cosmochim. Acta 65(21) (2001) 3671-3681.

[27] E.H. Oelkers, General kinetic description of multioxide silicate mineral and glass dissolution, Geochim. Cosmochim. Acta 65(21) (2001) 3703-3719.

[28] S.R. Gislason, E.H. Oelkers, Mechanism, rates, and consequences of basaltic glass dissolution: II. An experimental study of the dissolution rates of basaltic glass as a function of pH and temperature, Geochim. Cosmochim. Acta 67(20) (2003) 3817-3832.

[29] P.M. Dove, N. Han, A.F. Wallace, J.J. De Yoreo, Kinetics of amorphous silica dissolution and the paradox of the silica polymorphs, Proceedings of the National Academy of Sciences 105(29) (2008) 9903-9908.

[30] P.M. Dove, N. Han, J.J. De Yoreo, Mechanisms of classical crystal growth theory explain quartz and silicate dissolution behavior, Proceedings of the National Academy of Sciences 102(43) (2005) 15357-15362.

[31] S. Erdogan, P. Quiroga, D. Fowler, H. Saleh, R.A. Livingston, E.J. Garboczi, P.M. Ketcham, J.G. Hagedorn, S.G. Satterfield, Three-dimensional shape analysis of coarse aggregates: New techniques for and preliminary results on several different coarse aggregates and reference rocks, Cem. Concr. Res. 36(9) (2006) 1619-1627.

[32] S. Li, D.M. Roy, Investigation of relations between porosity, pore structure, and C1− diffusion of fly ash and blended cement pastes, Cem. Concr. Res. 16(5) (1986) 749-759.

[33] V. Ngala, C. Page, Effects of carbonation on pore structure and diffusional properties of hydrated cement pastes, Cem. Concr. Res. 27(7) (1997) 995-1007.

[34] T. Vuk, V. Tinta, R. Gabrovšek, V. Kaučič, The effects of limestone addition, clinker type and fineness on properties of Portland cement, Cem. Concr. Res. 31(1) (2001) 135-139.

[35] D.P. Bentz, G. Sant, J. Weiss, Early-age properties of cement-based materials. I: Influence of cement fineness, J. Mater. Civ. Eng. 20(7) (2008) 502-508.

[36] Z. Yang, X.-F. Peng, D.-J. Lee, M.-Y. Chen, An image-based method for obtaining pore-size distribution of porous media, Environmental Science & Technology 43(9) (2009) 3248-3253.

[37] Y. Niibori, M. Kunita, O. Tochiyama, T. Chida, Dissolution rates of amorphous silica in highly alkaline solution, Journal of Nuclear Science and Technology 37(4) (2000) 349-357.

[38] E.L. Cussler, Diffusion: mass transfer in fluid systems, Cambridge university press, 2009.

[39] H. Huang, Thermodynamics of autogenous self-healing in cementitious materials, PhD thesis, Delft University of Technology, Delft, 2014.

[40] C.J. Fell, H.P. Hutchison, Diffusion coefficients for sodium and potassium chlorides in water at elevated temperatures, Journal of Chemical & Engineering Data 16(4) (1971) 427-429.

[41] S.A. Socolofsky, G.H. Jirka, Environmental Fluid Mechanics Part I: Mass Transfer and Diffusion, Karlsruhe Institute of Technology, , 2002.